Accepted by the Astrophysical Journal

Chandra X-ray Observations of Pictor A: High Energy Cosmic Rays in a Radio Galaxy

A. S. Wilson[1], A. J. Young and P. L. Shopbell[2]

Astronomy Department, University of Maryland, College Park, MD 20742; wilson@astro.umd.edu, ayoung@astro.umd.edu, pls@astro.umd.edu

ABSTRACT

We report X-ray observations of the nearby, powerful radio galaxy Pictor A with the Chandra Observatory and optical and near uv observations of its western radio hot spot with the Hubble Space Telescope. X-ray emission is detected from the nucleus, a $1\farcm9$ (110 kpc) long jet to the west of the nucleus, the western radio hot spot some $4\farcm2$ (240 kpc) from the nucleus, and the eastern radio lobe. The morphology of the western hot spot is remarkably similar to that seen at radio and optical wavelengths, where the emission is known to be synchrotron radiation. The X-ray spectrum of the hot spot is well described by an absorbed power law with photon index $\Gamma = 2.07 \pm 0.11$. The X-ray jet coincides with a weak radio jet and is laterally extended by $\simeq 2\farcs0$ (1.9 kpc). The observed jet is up to $\simeq 15$ times brighter in X-rays than any counter jet, a difference ascribed to relativistic boosting as the western radio lobe is probably the closer. The jet's spectrum is well modelled by an absorbed power law with $\Gamma = 1.94^{+0.43}_{-0.49}$ and poorly fitted by a Raymond-Smith thermal plasma model.

The emission processes responsible for the X-rays are discussed in detail. The radio-optical spectrum of the hot spot breaks or turns down at 10^{13-14} Hz, and its X-ray spectrum is not a simple extension of the radio-optical spectrum to higher frequencies. Thermal models for the hot spot's X-ray emission are ruled out. Synchrotron self-Compton models involving scattering from the *known* population of electrons give the wrong spectral index for the hot spot's X-ray emission and are also excluded. A composite synchrotron plus synchrotron self-Compton model can match the X-ray observations but requires similar contributions from the two components in the Chandra band. We show that the hot spot's X-ray emission could be synchrotron self-Compton emission from a hitherto unobserved population of electrons emitting at low radio frequencies, but do not favor this model in view of the very weak magnetic field required.

---

[1]Adjunct Astronomer, Space Telescope Science Institute, 3700 San Martin Drive, Baltimore, MD 21218; awilson@stsci.edu

[2]Present address: Department of Astronomy, Mail Code 105-24, California Institute of Technology, Pasadena, CA 91125

For the jet, inverse Compton models require a magnetic field a factor of $\simeq$ 30 below equipartition, and ad hoc conditions to explain why the radio lobes are fainter than the jet in X-rays, but brighter in the radio.

Synchrotron radiation is the favored process for the X-ray emission. The expected synchrotron spectrum from relativistic electrons accelerated by strong shocks and subject to synchrotron radiation losses is in very good agreement with that observed for both the hot spot and jet. The possibility that the relativistic electrons result via photo-pion production by high energy protons accelerated in shocks (a 'proton induced cascade') is briefly discussed.

Subject headings: galaxies: active – galaxies: individual (Pictor A) – galaxies: jets – galaxies: nuclei – ISM: cosmic rays – X-rays: galaxies

1. Introduction

X-ray observations of radio galaxies are of value for several reasons. Low brightness radio lobes may be thermally confined by the hot, extended atmospheres in elliptical galaxies or clusters of galaxies and X-ray observations can provide the density, temperature and pressure of this gas, thus constraining the pressures of the relativistic gas and magnetic field in a lobe (e.g. Worrall & Birkinshaw 2000). High brightness regions, such as the hot spots in Fanaroff-Riley class II (FRII) radio galaxies, cannot be statically confined by thermal pressure and must be expanding and/or advancing away from the nucleus. If the motion is supersonic, such a feature must be preceded by a bow shock in the surrounding medium. The effect of bow shocks on the ambient gas may be identifiable in thermal X-ray emission, depending on the run of temperature and density in the post-shock gas (e.g. Clarke, Harris & Carilli 1997). Thermal X-rays may also be detectable from radio jets and lobes themselves if they entrain and shock surrounding gas (e.g. de Young 1986). The relativistic particles responsible for the synchrotron radio emission must also radiate through inverse Compton scattering of ambient photons (such as the microwave background and the starlight of the galaxy) or the synchrotron photons themselves. This inverse Compton radiation is expected to be spread over a wide range of frequencies, including the X-ray band. Detection of both synchrotron and inverse Compton radiation provides a direct measurement of the magnetic field in the emitting region (e.g. Harris, Carilli & Perley 1994), allowing a check on the common assumption of equipartition of energy between cosmic rays and magnetic fields. Lastly, synchrotron X-ray emission may be observable if electrons and/or positrons of sufficiently high energy are present, a finding which would provide important clues about the origin of the relativistic particles in these objects. For these reasons, we have begun a program of imaging and spectroscopy of radio galaxies with the Chandra X-ray Observatory.

Pictor A is the seventh brightest extragalactic radio source in the sky at 408 MHz (Robertson

1973[3]), and the most powerful radio galaxy ($P_{408MHz} = 6.7 \times 10^{26}$ W Hz^{-1} for z = 0.035, $q_0 = 0$ and $H_0 = 50$ km s^{-1} Mpc^{-1}) with z < 0.04. The best radio maps (Perley, Röser & Meisenheimer 1997, hereafter PRM) reveal two round, diffuse lobes with very much brighter radio hot spots on the sides away from the nucleus, corresponding to an FRII classification. The total angular diameter of the radio emission is about $7\rlap{.}'6$ (430 kpc). The western hot spot, some $4\rlap{.}'2$ (240 kpc) from the nucleus, is a remarkable object, being amongst the brightest of radio hot spots in radio galaxies and quasars. PRM have found a very faint radio jet extending from the compact, flat spectrum (cf. Jones, McAdam & Reynolds 1994) nuclear core to the western hot spot. Recently, VLBI observations (Tingay et al. 2000) have revealed a milli arc second- (pc-) scale nuclear radio jet which is approximately aligned with the large-scale radio jet. Simkin et al. (1999) have reported an optical continuum extension $\simeq 0\rlap{.}''1$ (95 pc) to the W of the nucleus and the direction to this extension is also roughly aligned with the larger scale radio jet.

Röser & Meisenheimer (1987) discovered optical emission from the western hot spot. This emission has a featureless continuum, is strongly polarized and thus of synchrotron origin. These authors also found a marginal detection of the hot spot at X-ray wavelengths in an Einstein IPC observation. Further observations of the hot spot in the infrared have been reported by Meisenheimer, Yates & Röser (1997). The overall spectrum of the western hot spot conforms to a power law with index $\alpha = 0.74$ ($S \propto \nu^{-\alpha}$) from 327 MHz to $\sim 10^{14}$ Hz, where the spectrum turns down (see Fig. 2i of Meisenheimer, Yates & Röser 1997). The morphologies of the hot spot are very similar at radio and optical wavelengths, with a bright, compact, leading "core" and a fainter, following "filament", which extends $\simeq 15''$ (14 kpc) more or less perpendicular to a line joining the hot spot to the nucleus (PRM). Fainter radio emission associated with the hot spot is also seen to the E and NE of the optical and radio filament, the overall angular extent of the radio hot spot being $\simeq 25''$ (24 kpc). The radio to optical spectrum of the "filament" is somewhat steeper ($\alpha_{opt}^{3.6cm} = 0.98$) than that of the bright, compact region ($\alpha_{opt}^{3.6cm} = 0.87$). Optical imaging and polarimetry of the bright part of the hot spot with the Hubble Space Telescope (Thomson, Crane & Mackay 1995) confirms the high polarization ($\gtrsim 50\%$) and resolves the hot spot into highly polarized "wisps" elongated nearly perpendicular to the nucleus - hot spot line.

The nucleus of Pictor A has long (Schmidt 1965; Danziger, Fosbury & Penston 1977) been known for its strong emission-line spectrum, with broad wings to both forbidden and permitted lines. Double-peaked, very broad Balmer lines were discovered in 1993/1994 (Halpern & Eracleous 1994; Sulentic et al. 1995); these double-peaked lines were not present in 1983. Such line profiles are commonly interpreted as emission from an accretion disk (e.g. Storchi-Bergmann et al. 1997). The nucleus of Pictor A is a strong X-ray source; the spatially integrated emission observed with ASCA has a power-law continuous spectrum and no evidence for an Fe Kα line (Eracleous & Halpern 1998). Further observations of the X-ray spectrum of Pictor A have been reported recently by Padovani et al. (1999) and Eracleous, Sambruna & Mushotzky (2000).

[3]Robertson's catalog excludes Cyg A on account of its low galactic latitude

We selected Pictor A for observation with Chandra because of the X-ray emission from the western hot spot, tentatively detected with the Einstein IPC and confirmed by us through an inspection of an archival ROSAT PSPC observation. Further, the optical synchrotron emission from the hot spot is of sufficient extent ($\sim 15''$) to be well resolved by Chandra, making this object a prime candidate for the study of high energy processes in the hot spots of powerful radio galaxies. In addition to the Chandra observations, we also report analysis of archival Hubble Space Telescope (HST) optical and near uv imaging observations of the western hot spot.

Section 2 describes the observations and their reduction while Section 3 presents the results. In Section 4, we discuss the orientation of the radio source and the processes responsible for the X-ray emission of the western hot spot and jet. Concluding remarks are given in Section 5.

2. Observations and Reduction

2.1. Chandra X-ray Observations

Pictor A was observed by the Chandra X-ray Observatory on Jan 18 2000 (sequence number 700018, obsid 346) using the Advanced CCD Imaging Spectrometer (ACIS) spectroscopic array, which provides excellent spatial resolution ($\leq 1''$) with medium spectroscopic resolution ($\simeq$ 130 eV FWHM at 1 keV) at the aim point on chip S3 (back illuminated). In order to obtain good spatial resolution on the western hot spot while retaining excellent resolution on the nucleus, the latter was placed about $1'$ from the aim point in the direction towards the S3/S2 chip boundary (the –Y direction). The nucleus was thus about $1'$ from the S3/S2 boundary. The western hot spot was $\simeq$ $3\overset{'}{.}5$ from the aim point and also on chip S3. The spatial resolution at the nucleus is barely different from the optimal, while that at the hot spot is $1\overset{''}{.}2 \times 1\overset{''}{.}9$ FWHM. The eastern radio lobe is partly on S3 and partly on S2 (front illuminated). The total integration time ("Good Time Intervals") was 26.177 ksecs, taken with the default frame time of 3.2 sec. There were no flares in the background count rate, which remained constant at 1.4 counts per second over the S3 chip.

The data were processed using version R4CU4UPD4.2 of the pipeline software, and we have used the updated gain file acisD1999-09-16gainN0003.fits. The data extraction and analysis have been performed using version 1.1 of the CIAO software and version 11.0 of XSPEC.

In order to create an X-ray image covering the whole radio source (shown as Fig. 1), it was necessary to remove CCD artifacts that take the form of broad, linear features along the readout direction in chips S2 and S3. This was accomplished by first copying a spatial subsection of the level 2 events file and rotating it by -37.6°, so that the axis of the S array ran horizontally. The image was then smoothed with a Gaussian with $\sigma = 1\overset{''}{.}0$ and the average of the rows computed, including rejection of those pixels in each column which were more than 2σ from the mean for that column. The average of the rows was then subtracted from each row. Finally, the image was rotated by +37.6°, so the rows and columns corresponded to the cardinal directions. This process not only removed most of the linear artifacts, but also the 'streak' from the very strong nuclear source that results from its readout and much of the differences in background level between the two chips.

To derive the X-ray spectrum of the hot spot, counts were extracted from a rectangular region $15'' \times 20''$ in extent which includes all of the X-ray emission from the hot spot. Background counts were taken from an area of identical shape offset to the west. Other extraction regions were tried for the background but no significant changes were seen. We obtain a total of 3413 counts from the hot spot and 125 from the background. Response and auxiliary response files were created using the standard CIAO tools. The source counts were grouped so that each channel has at least 25 counts so that the χ^2 fitting in XSPEC is meaningful.

We followed a similar procedure to obtain the X-ray spectrum of the jet. Counts were taken from a rectangular region $103'' \times 2\farcs4$ that contains the whole jet and minimises background (the $\sim 10''$ gap between the nucleus and the eastern end of the jet was excluded). The background was taken from adjacent regions, and no significant difference was found for the jet's spectrum when using different regions for the background. We obtain a total of 481 counts from the jet and 240 from the background. The X-ray response of the CCDs depends on the location of the source on the chip. To account for this, the back-illuminated S3 chip has 1024 individual calibration measurements (256 per node) arranged in a 32×32 grid covering the face of the chip. This oversamples the variation in the response of the CCD, and a single calibration measurement may be used for a source extending up to 64×64 pixels (approximately $32'' \times 32''$). The X-ray jet extends 228 pixels ($1\farcm9$) from the nucleus, so we divided it into four sections, each of which has a separate response. We also note that the jet crosses a 'node boundary' (the division between sections of the chip that have different read-out amplifiers), and that the response may vary sharply across this boundary. To avoid any problem with this, we also divided the jet at the node boundary so as not to mix events collected by different nodes.

Each of the four spectra were grouped to give each channel at least 20 counts so that χ^2 fitting is valid. These spectra were fitted simultaneously in XSPEC with each spectrum having its own background, response and auxiliary response file. The spectral properties are assumed to be constant along the length of the jet so the parameters in the fit are tied together with the exception of their normalizations.

One drawback of treating the jet in this way is that the individual spectra will have extremely low count rates, and fitting may only be valid over a limited range in energy. It is also difficult to produce clear figures of the spectral fits since there are four almost coincident data sets. To overcome these problems the entire jet spectrum may be treated as a single data set, using an 'averaged' response function that is the photon weighted average of the four individual responses. We use PI spectra, which are gain corrected, to minimize the effect of collecting photons from two different nodes. The results we obtain using this technique are equivalent, within the errors, to those obtained through fitting the spectra individually.

2.2. HST Optical and Near UV Observations

Six images of the western hot spot were obtained on August 19, 1995 as part of GO program #5931 (PI Meisenheimer), three each in the F300W and F622W broadband filters. The images in each filter were dithered by several arc seconds in order to improve the effective spatial resolution of the images on the PC chip. However, the lack of duplicate exposures at each pointing, i.e., no CR-SPLIT, and the paucity of sources in the field greatly complicated attempts at alignment of the images. Instead, a number of cosmic rays were cleaned from each image by hand, and then the total number of sky-subtracted counts in the hot spot was determined for each frame. After averaging the results for each filter, the counts were converted to units of flux using the SYNPHOT package in IRAF[4]. The derived values, as plotted in Fig. 6, are 30 μJy and 104 μJy for the F300W and F622W filters, respectively. The errors in these values have been estimated at 10%.

3. Results

3.1. Overall Morphology

A low resolution X-ray image, covering all of the radio emitting regions and with selected VLA radio contours (from PRM) overlaid, is shown in Fig. 1, while a full resolution X-ray image of the nucleus and structure to the west of the nucleus is shown in Fig. 2. The brightest X-ray source is associated with the nucleus of the galaxy. The position of this source, as measured with the Chandra aspect system, is within $2''$ of the radio and optical nuclear positions given by PRM. The nucleus is so bright in X-rays that it suffers from strong "pile up", so no useful spatial or spectroscopic information can be obtained from this exposure; a Chandra observation with a shorter frame time is scheduled to obtain a reliable nuclear spectrum. A linear feature, visible in both figures, extends $1\overset{\prime}{.}9$ (110 kpc) westward from the nucleus and is spatially coincident with the faint radio jet (PRM); we shall refer to this feature as the "X-ray jet". The X-ray jet "points" at the western hot spot, which is $4\overset{\prime}{.}2$ (240 kpc) from the nucleus. When the nuclear X-ray source is shifted slightly to coincide with the nuclear radio source, the peak of the X-ray emission from the hot spot is within $1''$ of its radio peak. There is also evidence for faint, diffuse X-ray emission around the nucleus and extending $\sim 1'$ from it, but more sensitive observations are needed to confirm this component.

Faint X-ray emission extends eastwards from the nucleus to the two eastern radio hot spots, $3\overset{\prime}{.}1$ and $3\overset{\prime}{.}4$ from the nucleus (Fig. 1). This faint X-ray emission is seen to brighten somewhat within $\sim 1'$ of these hot spots. There are also four compact X-ray sources within the brightest radio contour around the eastern hot spots; none of these X-ray sources coincides with either radio hot spot. Lastly, we point out a faint ($40 - 50$ counts above the background), compact X-ray source $323''$ E

[4]IRAF is distributed by the National Optical Astronomy Observatories, which are operated by the Association of Universities for Research in Astronomy, Inc., under cooperative agreement with the National Science Foundation.

of the nucleus at $\alpha = 05^h\ 20^m\ 20^s.0$, $\delta = -45^\circ\ 47'\ 44''$ (J2000). This X-ray source is beyond the eastern radio lobe, but it lies in p.a. 101° from the nucleus, a direction which is precisely opposite to the direction to the western hot spot (p.a. 281°). Examination of the Digital Sky Survey reveals a faint point source within $\sim 1''$ of this position, almost at the limit of the SERC-J Survey (we estimate $m_{\rm SERC-J} \approx 21$), and marginally detected in the Second Epoch Southern (UK Schmidt) survey. It is unclear whether this compact X-ray source is related to Pictor A.

3.2. The Western Hot Spot

3.2.1. Morphology

Images of the western hot spot at radio (PRM), optical (Röser 1989; PRM) and X-ray wavelengths with similar resolutions are shown in Fig. 3. As described in the Introduction, the radio and optical hot spots have a very similar morphology. In a higher resolution ($0''\!.45 \times 0''\!.09$) radio image (Fig. 19 of PRM), the bright "core" is found to have a sharp leading (i.e. away from the nucleus) edge, with a slower decline on the side towards the nucleus. Behind this bright region is a linear feature elongated in p.a. 32° (Fig. 3), referred to as the "filament" by Röser & Meisenheimer (1987) and the "plateau" by PRM.

The overall X-ray morphology is remarkably similar to the radio and optical, with both the "core" and the "filament" detected. Much of the apparent elongation of the brighter part of the "core" of the X-ray hot spot (Fig. 3) reflects the shape of the point spread function (psf). Fig. 4 compares profiles along the major and minor axes of the hot spot through both the hot spot and the model psf at the location of the hot spot. At half maximum, the hot spot is somewhat wider than the model, but the model psf does not include broadening by imperfections in the aspect solution. In order to assess the reliability of the model psf, we have compared a compact X-ray source (visible in Fig. 1) some $152''$ from the nucleus in p.a. 40° with the Chandra model psf at this location. The observed profile of this source (which is at a similar distance from the aim point as the hot spot) is in good agreement with the model psf, but broader by $0''\!.2$ at the half power point. This number is similar to the excess broadening of the hot spot over the model psf along its minor axis (Fig. 4), suggesting that the brighter part of the hot spot is unresolved in this direction. The excess FWHM of the hot spot over the psf along its major axis (Fig. 4) is somewhat larger. Nevertheless, we feel that caution is necessary, since other effects (e.g. the motion of the source on the detector during an observation) could lead to further broadening compared with the model psf. The conservative conclusion is that the brightest part of the "core" is marginally resolved or unresolved in X-rays.

There are, however, clear indications of structure in the hot spot at lower brightness levels. As in the radio, the X-ray core has a sharper edge away from the nucleus than towards it. A narrow "ridge" extends $\simeq 3''\!.5$ (3.4 kpc) in p.a. 108° (the general direction towards the nucleus) from the hot spot peak. A weaker feature some $6''$ (5.7 kpc) SSW of the core and elongated towards p.a. 279°, is seen in both the radio and X-ray images. In conclusion, when the small differences in resolution of the X-ray and radio images (Fig. 3) are taken into account, the X-ray and radio morphologies are remarkably similar. This morphological similarity indicates that the X-ray, optical and radio-emitting regions are physically co-spatial and argues that the X-ray emission does not originate from a bow shock ahead of the radio hot spot.

3.2.2. X-ray Spectrum

The X-ray spectrum of the hot spot has been modelled in various ways. A hot plasma with solar abundances and in collisional equilibrium ("Raymond-Smith" model) provides a poor fit to the data (Table 1) and can be ruled out. If the abundances of all elements heavier than helium are allowed to vary, we find that an abundance of $\lesssim$ 10 per cent solar is needed for this thermal model to provide an acceptable description of the data. However, this model (Table 1) requires a hydrogen column well below the Galactic value of $N_H = 4.2 \times 10^{20}$ atoms cm^{-2} towards Pictor A (Heiles & Cleary 1979), and is thus implausible. Fixing the column at the Galactic value while allowing the abundances to vary leads to a poor fit (Table 1). Further, we shall argue in Section 3.2.3 that a thermal model can be excluded on grounds that the required gas density is so high that the radio emission would be Faraday depolarized, contrary to observation. Lastly, a power law of photon index $\Gamma = 2.07^{+0.11}_{-0.11}$ absorbed by a column density of solar abundance gas $N_H = (7.1^{+2.3}_{-2.3}) \times 10^{20}$ atoms cm^{-2} provides an excellent description of the spectrum (Table 1, Fig. 5). This column density is only slightly greater than the Galactic column density towards Pictor A, suggesting that the interstellar medium of our Galaxy is responsible for most of the observed absorption. The unabsorbed flux and luminosity of the western hot spot in the 2 - 10 keV band are 3.1×10^{-13} erg cm^{-2} s^{-1} and 1.7×10^{42} erg s^{-1}, respectively.

3.2.3. X-ray Emission Mechanism

We first evaluate the thermal model. If we assume a representative intrinsic dimension of 1.9 $\times$ 0.9 $\times$ 0.9 kpc (i.e. $2'' \times 1'' \times 1''$), as suggested for the bright "core" by the X-ray image (Figs 3 and 4), the required gas density for the best fitting Raymond-Smith model is $n_e \simeq 3$ cm^{-3}. Because the X-rays come from the same general region of space as the radio and optical emission (Fig. 3), we may estimate the magnetic field in this putative thermal gas from the synchrotron emission. For an equipartition magnetic field of 4.7×10^{-4} gauss (obtained assuming a total cosmic ray energy equal to twice that of the electrons, $\alpha = 0.74$ [Meisenheimer, Yates & Röser 1997], lower and upper cut-off frequencies 10^7 and 10^{14} Hz, respectively, and an emitting volume corresponding to the size of the radio core - 760 $\times$ 190 $\times$ 190 pc [$0''.8 \times 0''.2 \times 0''.2$]), the rotation measure through the hot spot is expected to be $\simeq 6 \times 10^5$ rad m^{-2}. If the larger volume adopted above for the X-ray source is used to calculate the equipartition field, a value of 1.4×10^{-4} gauss and a rotation measure through the hot spot of $\simeq 2 \times 10^5$ rad m^{-2} are found. In contrast, the high polarization observed at 6 cm implies a rotation measure internal to the hot spot < 900 rad m^{-2} ($n_e < 0.014$ cm^{-3}), a factor of $\simeq 200$ lower than required for thermal emission. If the 20 cm polarization is used, the upper limit on rotation measure and density are an order of magnitude smaller, but the hot spot is not well resolved at this wavelength. We thus conclude that our upper limit to the gas density renders a thermal model untenable. This conclusion could be wrong if either a) the magnetic field has a preferred direction but many reversals; such a field structure can provide the high observed synchrotron polarization but gives little Faraday rotation, or b) the thermal gas is actually in small, dense clumps with a small covering factor. We favor neither of these: the field structure of a) is physically implausible, and it is very improbable that thermal gas of density 3 cm^{-3}, let alone the higher density required if the gas is clumped, exists 240 kpc from the Pictor A galaxy. Another argument for a low gas density in the hot spot comes from the photoelectrically absorbing column. Most or all of this column comes from gas in our Galaxy; any contribution from other regions is $< 3 \times 10^{20}$ atoms cm^{-2} (Table 1). If spread uniformly throughout the hot spot "core" of average diameter ~ 1 kpc, the density is < 0.1 cm^{-3} (as long as electrons are not stripped from the K shells of the relevant elements), a factor of 30 below the density needed for thermal emission. In summary, our finding (Section 3.2.2) that a thermal model provides a poor description of the X-ray spectrum, and the upper limits to the gas density from the limits on Faraday depolarization and the absorbing column, rule out a thermal model of the X-rays from the hot spot We conclude that the X-rays are non-thermal in origin and discuss relevant models in Section 4.2.2.

3.3. The X-ray Jet

3.3.1. Morphology

The X-ray jet extends $1\overset{\prime}{.}9$ (110 kpc) westward from the nucleus in p.a. 281° (Fig. 2). This direction is only 1° away from that quoted for the radio jet out to $3'$ (170 kpc) from the nucleus (PRM). Such a difference in p.a. is within the errors of measurement, so we can conclude that the X-ray and radio jets are coincident.

The profile of X-ray emission along the jet, shown in Fig. 6, consists of a number of 'knots', the brightest of which is $30''$ from the nucleus. In Section 4.1, we shall argue that the western radio lobe is the nearer. The ratio of the X-ray fluxes of the western and eastern jets, using the brightest part of the western jet, is more than a factor of 10 (Fig. 6), suggesting relativistic boosting, as discussed in Section 4.3.2.

We have compared the transverse profiles across the jet with the expected psf. After deconvolution from the psf, the jet is found to be transversely extended. The width of the jet varies somewhat along its length, but its typical FWHM = $2\overset{\prime\prime}{.}0$ (1.9 kpc). We are confident of this transverse extent because: a) the profile of the compact source $152''$ from the nucleus in p.a. 40° agrees well with the expected psf at its location (Section 3.2.1), and b) the linear feature that results from the CCD readout of the strong nuclear source gives a measure of the 1d psf at the nucleus; this feature is much narrower than the jet. These arguments show that the measured jet width is not a result of poor aspect solution or focus.

The jet is so faint in the radio that it is difficult to measure its width. PRM state "no accurate estimate of the jet's width is possible, but it is clearly not greatly resolved by the 7.″5 beam". Thus the upper limit to the radio width is consistent with the X-ray width.

3.3.2. X-ray spectrum

Given the low count rate, the background begins to dominate above 2.5 keV. The same models as used for the hot spot were tried for the jet (Table 2). The Raymond-Smith thermal models provide a poor fit to the spectrum, even when the metal abundance is a free parameter. An absorbed power-law model provides an excellent description of the spectrum of the jet (Fig. 7). The absorbing column density ($N_{\rm H} = 5.8^{+6.8}_{-5.6} \times 10^{20}$ atoms cm^{-2}) and photon index ($\Gamma = 1.94^{+0.43}_{-0.49}$) are similar to those found for the hot spot. Again we conclude that most of the absorption occurs in the interstellar medium of our Galaxy. The unabsorbed 2 - 10 keV flux and luminosity of the jet are 2.5×10^{-14} erg cm^{-2} s^{-1} and 1.4×10^{41} erg s^{-1}, respectively.

3.3.3. X-ray Emission Mechanism

Even if the metal abundance is left as a free parameter, a Raymond-Smith thermal plasma model provides a poor fit to the jet's spectrum (Section 3.3.2, Table 2). Since there is no information on the radio polarization of the jet, we cannot argue against a thermal model on grounds of internal Faraday depolarization, as we did for the western hot spot. The X-ray absorbing column within the jet must be $\lesssim 8.4 \times 10^{20}$ atoms cm^{-2} (the maximum allowed column [Table 2] minus the Galactic column), which implies a density $n_e < 0.15$ cm^{-3}. For the observed X-ray emission to be thermal, the average density of hot gas in the jet (taken to be a cylinder of radius 1″ and length 1.′9) is $n_e \simeq 0.05$ cm^{-3}, compatible with the limits from the absorbing column. Thus the only argument against thermal emission is the poor description of the spectrum by a Raymond-Smith model. We will discuss non-thermal models for the jet in Section 4.3.2.

4. Discussion

4.1. Orientation of the Radio Source

The projected distance, d_w, of the W radio hot spot of Pictor A from the nucleus is larger than that, d_e, of the E radio hot spots. This observation is consistent with the W radio lobe being the nearer one, since the extra light travel time to the more distant lobe implies that it is seen at an earlier phase in its motion away from the nucleus and thus appears closer to the nucleus. Further, the east lobe is more depolarized than the west at long radio wavelengths (PRM), again suggesting that the W lobe is the nearer (Laing 1988). Both the radio and X-ray jets of Pictor A are seen on the W side of the nucleus. These considerations strongly suggest that the jet sidedness is a result of relativistic boosting.

The angle of the source axis to the line of sight is, of course, unknown, but can be estimated from $\mathrm{d_w}$ and $\mathrm{d_e}$ if the source is assumed to be intrinsically symmetric, since

$$\frac{d_{\mathrm{w}} - d_{\mathrm{e}}}{d_{\mathrm{w}} + d_{\mathrm{e}}} = \beta \cos\theta \tag{1}$$

where $\beta = \mathrm{V/c}$, V is the velocity with which the hot spots are receding from the nucleus and θ is the angle between the radio axis and our line of sight. A recent study (Arshakian & Longair 2000) has found the mean value of β in a sample of FRII radio galaxies to be 0.11 $\pm$ 0.013. For Pictor A, we may then write

$$\cos\theta = 0.92 \left(\frac{\mathrm{V}}{0.11\mathrm{c}}\right)^{-1} \tag{2}$$

so $\theta = 23^\circ$ if V = 0.11 c. In view of its sensitivity to V and the assumption of symmetry, this value of θ should not be taken too seriously.

The radio lobes are remarkably round and are quite well separated in the VLA images (PRM), although joined by a 'waist' near the nucleus. This morphology suggests that θ is larger than 23°. A larger value is also suggested by the fact that the hot spots project further away from the nucleus than the outer edges of the lobes themselves.

4.2. The X-ray Emission of the Western Hot Spot

4.2.1. Radio to X-ray Spectrum

Fig. 8 shows the broad band spectrum of the western hot spot. All of the radio points and most of the optical and near infrared ones were taken from Meisenheimer, Yates & Röser (1997). To these we added the flux densities at $\simeq$ 2900 Å and $\simeq$ 6200 Å obtained from our analysis of archival HST data (Section 2.2). These HST values may underestimate the true flux densities as some of the emission is resolved out. Also included is the original estimate of the X-ray flux density from the Einstein Observatory (Röser & Meisenheimer 1987) and the Chandra-measured intrinsic spectrum. The Einstein point is a factor of $\sim$ 2 higher than the Chandra measurement; this may be a result of partial blending of the hot spot with the much stronger nuclear source in the low spatial resolution Einstein observation. The radio spectrum of the hot spot is well described by a power law with α = 0.740 $\pm$ 0.015 (Meisenheimer, Yates & Röser 1997), but there must be a break or turnover in the spectrum at 10^{13-14} Hz to accommodate the near infrared and optical measurements. It is also apparent that the X-ray spectrum is not a simple extension of the radio and optical measurements to higher frequencies. The luminosities of the radio to optical and the X-ray components are given in Table 3.

4.2.2. Non-Thermal Models

Inverse Compton and Synchrotron Emission from the Radio and Optical-Emitting Electron Population

It has long been realised that the outward motion of hot spots in FRII radio galaxies is sub-relativistic. The most recent work (Arshakian & Longair 2000) obtains a mean outward velocity of 0.11c ± 0.013c. While the velocity of a hot spot in any individual object is uncertain, we shall neglect boosting or diminution of the hot spot fluxes by bulk relativistic motion.

The broad-band spectrum (Fig. 8) shows that the X-ray emission of the western hot spot cannot be synchrotron radiation from a high energy extension of the population of electrons responsible for the radio to optical synchrotron radiation. It is, therefore, natural to consider inverse Compton scattering for the X-ray emission. In the bright core of the hot spot, the radiant energy density (ϵ_{rad}) of the synchrotron radiation dominates that of the microwave background radiation and the galaxy starlight (Table 3), so it is appropriate to consider a synchrotron self-Compton model[5]. When the scattering electrons follow a power-law distribution in γ (= $\mathrm{E/mc^2}$), $\mathrm{n}(\gamma) = \mathrm{n}_{e_0}\gamma^{-\mathrm{p}}$ over all γ, then the inverse Compton spectrum is a power law with a spectral index $\alpha_C = (\mathrm{p}-1)/2$, the same index as the synchrotron spectrum.[6] The fact that the radio ($\alpha_{rad} = 0.740 \pm 0.015$) and X-ray ($\alpha_{X-ray} = 1.07^{+0.11}_{-0.11}$) spectral indices are different then suggests difficulties with an inverse Compton model. However, in reality, the electron energy spectrum is a power law over only a certain range of γ (from γ_{min} to γ_{max}), and the synchrotron spectrum is a power law over only a certain range of ν (from $\nu_{s,min}$ to $\nu_{s,max}$). These limited ranges yield "end effects" in synchrotron self-Compton spectra: the inverse Compton scattered spectra must turn down below $\nu_{c,min} \sim 4\gamma^2_{min}\nu_{s,min}$ and above $\nu_{c,max} \sim 4\gamma^2_{max}\nu_{s,max}$ (e.g. Blumenthal & Gould 1970; Rybicki & Lightman 1979). Further, the synchrotron self-Compton spectrum is no longer an exact power law between these limits.

In order to provide a more realistic evaluation of inverse Compton and synchrotron self-Compton models, we have performed numerical calculations of spectra in spherical geometries using the computer code of Band & Grindlay (1985, 1986), which was kindly provided by Dan Harris. Given the observed radio – optical spectrum (Fig. 8), we have assumed a power law elec-

---

[5] In the "filament", the energy densities of the synchrotron radiation and the microwave background are comparable.

[6] Because we are concerned with only scattered photons below an energy of 10 keV, we assume Thomson scattering throughout i.e. $\gamma h\nu_S \ll mc^2$, where ν_S is the frequency of the synchrotron photon and mc^2 is the rest mass energy of the electron.

tron spectrum with $p = 2.48$ from γ_{min} to γ_{max}. The magnetic field is treated as a variable. We first computed a synchrotron self-Compton spectrum which passes through the Chandra-measured flux (model 1). This was achieved for a magnetic field strength of 3.3×10^{-5} gauss, a factor of 14 below the equipartition field in the radio "core" of the hot spot (Table 4). However, the predicted spectrum is similar to that of the radio source and does not match the measured X-ray spectrum (Fig. 8).

As an alternative to reducing the field strength, the power radiated in inverse Compton radiation could be increased by increasing the radiation density. The nucleus of Pictor A might emit a narrow, collimated beam of radiation (like those inferred to be present in BL Lac objects) along the axis of the jet. This beam could illuminate the hot spot, but be invisible to us. However, an (isotropic) nuclear luminosity of 1.6×10^{48} erg s^{-1} is needed merely to *equal* the radiant energy density in synchrotron radiation in the core of the hot spot. The (isotropic) nuclear luminosity would have to be $\simeq 1.5 \times 10^{50}$ erg s^{-1} to provide sufficient radiation for the hot spot to radiate the observed X-ray flux by inverse Compton scattering if the field has its equipartition value. This luminosity is unreasonably large.

An alternative is that the X-rays are a combination of synchrotron and inverse Compton radiation. In model 2, we assumed that the turnover in the synchrotron spectrum at 10^{13-14} Hz is an effect of synchrotron losses on a continuously injected electron spectrum with energy index $p =$ 2.48. The assumed electron spectrum is thus a broken power law (Kardashev 1962):

$$n_e = n_{e_0}\gamma^{-p} \quad \gamma \ll \gamma_{\rm break} \tag{3}$$

$$n_e = n_{e_0}\gamma_{\rm break}\gamma^{-(p+1)} \quad \gamma \gg \gamma_{\rm break} \tag{4}$$

The synchrotron spectrum then has an index $\alpha = 0.74$ well below the break and $\alpha = 0.74 + 0.5 = 1.24$ is expected well above it (dotted line in Fig. 8). By adding this spectrum to the predicted synchrotron self-Compton component for a magnetic field of 5.3×10^{-5} gauss (dot-dashed line in Fig. 8), which is again well below equipartition, we obtain the solid line in Fig. 8, which is a good description of the Chandra spectrum. The parameters of model 2 are given in Table 4. Because the energy density in magnetic field is $\gtrsim$ an order of magnitude larger than the synchrotron radiation density, the power in the first order synchrotron self-Compton component is less than that in the synchrotron radiation (e. g. Rees 1967). Further, the second order scattered component is even weaker (3 orders of magnitude below the first order radiation in the Chandra band).

Assuming that the electrons are continuously accelerated in the hot spot, we may interpret the turnover frequency as the frequency at which the "half-life" to synchrotron losses of the radiating electrons is equal to their escape time from the hot spot. For the field of 5.3×10^{-5} gauss needed to match the X-ray spectrum, electrons radiating at 10^{14} Hz have a synchrotron "half-life" of $\simeq 10^4$ yrs. For a hot spot radius of $\simeq 250$ pc, the corresponding streaming velocity of the relativistic electrons is $\simeq 0.1$c. The problem with model 2 is the fine tuning needed: synchrotron and synchrotron self-Compton emission must be present in the Chandra band with comparable fluxes.

Inverse Compton and Synchrotron Emission from Hypothetical New Electron Populations

In the previous subsection, we showed that the X-ray emission is so strong that the magnetic field in the hot spot must be a factor of $\sim$ 14 below equipartition if the X-rays are produced by inverse Compton scattering from the electrons that generate the *observed* radio emission. Even then, the observed X-ray spectrum is different to the predicted one (Fig. 8), and so this model (model 1, Table 4) may be ruled out. The other process capable of generating the observed X-rays is synchrotron radiation. However, the X-ray emission of the hot spot is not a smooth continuation of the radio – optical synchrotron spectrum. In model 2, we contrived to fit the X-ray spectrum by a combination of synchrotron emission from an extension of the radio-optical spectrum and synchrotron self-Compton from the radio-optical synchrotron-emitting electrons. In view of the unsatisfactory nature of these models, we now consider inverse Compton and synchrotron models involving hypothetical new electron populations.

i) X-rays as inverse Compton radiation

For a successful inverse Compton scattering model, a low energy population of relativistic electrons with an index of the energy spectrum p $\simeq 2\alpha_X + 1$ is needed. The required value of p is thus $\mathrm{p_{hs}} \simeq 3.14^{+0.22}_{-0.22}$. Fig. 9 shows a model (model 3, Table 4) for the hot spot in which a synchrotron-emitting component with a larger spectral index than that observed in the radio has been added at low radio frequencies. The spectrum of the hot spot has not been measured below 327 MHz, but the extension of this hypothetical spectrum down to lower frequencies does not exceed the measured *integrated* flux density of Pictor A (the lowest such measurements are at $\sim$ 80 MHz, see PRM). It is envisaged that the population of electrons which emits the *observed* synchrotron radio emission is in a relatively strong (e.g. equipartition, Table 3) magnetic field, so that the synchrotron self- Compton emission from this *electron* population is negligible, as shown above. However, the observed radio-optical synchrotron *radiation*, as well as the radio synchrotron radiation of the hypothesised component, is available for scattering by the hypothetical low energy electron population. As can be seen from Fig. 9, the low energy electrons must radiate predominantly through the inverse Compton channel, requiring a very weak magnetic field (model 3, Table 4) which is $\sim$ 100 times weaker than the equipartition field in the core of the western hot spot. The calculation shows that the second order Compton scattered component is $\gtrsim$ 2 orders of magnitude weaker than the first order Compton scattered component in the Chandra band. We find that the spectrum of the low energy electrons has to be steep (p = 3.3) as shallower spectra (p < 3.3) cause the inverse Compton spectrum to increase above 10^{17} Hz, contrary to our X-ray observations. Taking this model to its extreme, the hypothetical electron population could be in a region free of magnetic field, and thus radiate no radio emission at all. This requirement for a weak or absent magnetic field associated with this population is difficult to understand in view of the finding that the X-ray, optical and radio emitting regions of the western hot spot are co-spatial (Section 3.2.1 and Fig. 3). High resolution radio observations at lower frequencies would provide stronger constraints on this model.

ii) X-rays as synchrotron radiation

Alternatively, the X-ray emission of the hot spot could be synchrotron radiation from a separate population of electrons. In such models (models 4a and b), the energy index of the X-ray emitting electrons would be $p_{hs} \simeq 3.14^{+0.22}_{-0.22}$, similar to the above inverse Compton model. In view of the short synchrotron loss times (a few years for a 5 keV-emitting electron in the equipartition field), the energy index at injection would be $p_{hs,inj} \simeq 2.14^{+0.22}_{-0.22}$ in a steady state, continuous injection model. The synchrotron break frequency must thus be below the X-ray band but above 10^{11} Hz (otherwise the emission would exceed the observed flux at the latter frequency). Models 4b and 4a (Table 4), in which we have adopted the equipartition field, represent these two extremes for the synchrotron break frequency, respectively. Thus, in both these models, the extrapolation of the X-ray spectrum to lower frequencies does not exceed the observed radio, infrared or optical flux. Interestingly, the required value of $p_{hs,inj}$ is the same to within the errors as the canonical index for particle acceleration by a strong shock (p = 2, e.g. Bell 1978; Blandford & Ostriker 1978). In this picture, electrons would have to be continuously reaccelerated by such shocks on pc scales.

4.3. The X-ray Emission of the Jet

4.3.1. Radio to X-ray Spectrum

Unfortunately, there is no information on the radio spectrum of the jet. We have only PRM's statement that the average excess brightness of the jet above the background lobe emission is estimated to be about 10 mJy ($7''.5$ beam)$^{-1}$ at λ 20 cm. Over the length of the detected X-ray jet, we then estimate a total 20 cm flux density of 152 mJy, with large uncertainties. The spectral index between 20 cm and 1 keV is $\alpha_{rx,jet} = 0.87$, which is similar to $\alpha_r = 0.85$, the spectral index for the *entire* radio source for $\nu > 400$ MHz (PRM). This value of $\alpha_{rx,jet}$ may also be compared with the index within the Chandra band of $\alpha_{x,jet} = 0.94^{+0.43}_{-0.49}$. Given the errors, it is not out of the question that the jet has a constant spectral index from GHz frequencies to 10 keV, but the radio spectrum is needed to check this. Simply joining the radio and X-ray flux densities with $\alpha_{rx} = 0.87$ implies a total optical magnitude for the jet of V $\simeq$ 23 mag, and an optical surface brightness of V $\simeq$ 29 mag (arc sec)$^{-2}$. The fact that the jet has not been detected in the optical is consistent with these numbers.

4.3.2. Non-Thermal Models

Some estimated parameters of the jet are given in Table 5. It is apparent that the microwave background radiation dominates the radiant energy within the jet, unless the radius of the radio synchrotron-emitting region is much smaller than the observed radius of the X-ray jet. The X-rays from the jet could be either inverse Compton or synchrotron radiation, which we discuss in turn.

Evaluation of these models is limited by our ignorance of the jet's radio spectrum. For concreteness, we shall adopt a jet radius of $1''$ (950 pc) for both the radio and X-ray emission.

i) X-rays as inverse Compton radiation

Adopting $\alpha_{\rm r,jet} = 0.87$, $S_{\rm jet,1.4GHz} = 152$ mJy for the part of the jet detected in X-rays (Section 4.3.1), and the equipartition field $H_{\rm jet} = 2.3 \times 10^{-5}$ gauss, the predicted inverse Compton scattered X-ray flux falls a factor of $\simeq 500$ below that observed. In order to match the observed X-ray flux, we need to reduce the magnetic field to $H_{\rm jet} \simeq 7 \times 10^{-7}$ gauss, a factor of $\simeq 30$ below equipartition. Alternatively, as for the hot spot, we could invoke a radiation beam from the nucleus to boost the radiation density in the jet. To obtain the observed X-ray flux from the jet while retaining the equipartition field requires an (isotropic) nuclear luminosity of $\sim 2 \times 10^{48}$ erg s^{-1}, which is implausibly high. We could also suppose, as we did for the hot spot, that the *observed* radio jet contains a stronger (e.g. equipartition) magnetic field and there is, in addition, a population of electrons in a weak or absent field. Because we do not know the radio spectrum of the jet, and have thus not been able to demonstrate that the radio and X-ray spectral indices are different, we cannot prove that the radio- and X-ray-emitting electrons represent different populations, as we could for the hot spot.

The above discussion neglects relativistic boosting or diminution by possible bulk relativistic motion of the jet. There is now a strong case for energy transport at bulk relativistic velocities to the hot spots in FRII sources (e.g. Bridle 1996). For emission which is isotropic in the rest frame and has a power law spectrum, the observed flux density, $F_\nu(\nu)$, is related to the flux density in the rest frame, $F'_\nu(\nu)$, by

$$F_\nu(\nu) \ = \delta^{3+\alpha} F'_\nu(\nu) \tag{5}$$

where $\delta = [\Gamma(1 \ - \beta \ \cos\theta)]^{-1}$, Γ is the Lorentz factor of the bulk flow, β is the bulk velocity in units of the speed of light, and θ is the angle between the velocity vector and the line of sight (e.g. Urry & Padovani 1995). This equation assumes that the emission comes from a discrete, moving source. For a smooth, continuous jet, the exponent $3+\alpha$ becomes $2+\alpha$ (Begelman, Blandford & Rees 1984). Equation (5) will describe relativistic boosting or diminution of the jet's synchrotron radiation, as long as that radiation is isotropic in the jet's rest frame.

As noted above (Table 5), the radiation density in the jet is dominated by the microwave background radiation, which is isotropic in the observer's frame and anisotropic in the rest frame of the jet. In this case, the principal dependence of the inverse Compton scattered radiation on θ is given by (Dermer 1995)

$$F_\nu(\nu) \ = \delta^{4+2\alpha} F'_\nu(\nu) \tag{6}$$

where an additional term which depends slowly on $\cos\theta$ has been omitted (Begelman & Sikora

1987; Dermer 1995). Retaining the discrete source model, the ratio of inverse Compton scattered to synchrotron flux is then

$$F_{C,\nu}(\nu)/F_{S,\nu}(\nu) \propto \delta^{1+\alpha}. \tag{7}$$

The orientation of the jet in Pictor A w.r.t. the line of sight is unknown. However, various considerations (Section 4.1) indicate that θ is at least 23° and probably larger. For this value of θ, the maximum possible value of $\delta^{1+\alpha}$ is ~ 5.8 (achieved at $\Gamma \simeq 2.6$), and this number is smaller for larger θ. We conclude that the factor of 500 discrepancy between the predicted and observed inverse Compton X-rays for an equipartition field cannot be resolved by differential relativistic boosting.

The following simple fact argues against inverse Compton scattering for the jet's X-ray emission: in the radio band, the western lobe dominates the jet, while in X-rays the converse is true. The ratio of the rates of energy loss to inverse Compton scattering and synchrotron radiation is

$$\frac{(\mathrm{dE/dt})_{\mathrm{IC}}}{(\mathrm{dE/dt})_{\mathrm{synch}}} = \frac{\epsilon_{rad}}{\epsilon_{mag}}. \tag{8}$$

The radiant energy density in both the jet and western lobe is dominated by the microwave background radiation. The equipartition magnetic field in the jet is $\simeq 2.3 \times 10^{-5}$ gauss (for $\mathrm{r_j} = 1''$, see Table 5) and that in the lobe is $\sim 5 \times 10^{-6}$ gauss. Thus one expects that the ratio $(\mathrm{dE/dt})_{\mathrm{IC}}/(\mathrm{dE/dt})_{\mathrm{synch}}$ should be larger for the lobe than the jet. Given that the lobe's radio synchrotron radiation overwhelmingly dominates that of the jet, the lobe's inverse Compton emission should dominate the jet by an even larger factor, contrary to observation. However, the jet's inverse Compton emission would be larger if either a) its magnetic field is well below equipartition, or b) a narrow beam of radiation is emitted by the nucleus along the jet, providing a larger ϵ_{rad} than the microwave background, as discussed above. Both of these possibilities are *ad hoc* and so we consider the prominence of the jet compared to the lobe in the Chandra image as an argument against inverse Compton scattering.

ii) X-rays as synchrotron radiation

As already noted, the available data are consistent with a single power law with $\alpha_{\mathrm{rx,jet}} = 0.87$ from 1.4 GHz to 10 keV. This is, however, an unlikely physical situation for a purely synchrotron spectrum in view of the short energy loss times of the X-ray emitting electrons to synchrotron and inverse Compton radiation. For electrons emitting synchrotron radiation at 1.4 GHz and 1 keV in the equipartition field of 2.3×10^{-5} gauss, the times to lose half their energy are $\simeq 4 \times 10^6$ and 300 yrs, respectively. If the energies of the radio-emitting electrons are not significantly reduced by synchrotron and inverse Compton losses, we would expect the radio spectrum to be flatter than the X-ray spectrum; in the simplest case involving continuous injection, $\alpha_{\mathrm{r,jet}} = \alpha_{\mathrm{x,jet}} - 0.5 \simeq 0.4$. It would thus be valuable to measure $\alpha_{\mathrm{r,jet}}$.

For a synchrotron model in which the electrons are isotropic in the frame of bulk jet motion, the observed ratio of flux in the approaching side of the jet to the receding side is given by

$$R = \frac{F_{\nu_{\rm app}}(\nu)}{F_{\nu_{\rm rec}}(\nu)} = \left(\frac{1+\beta\cos\theta}{1-\beta\cos\theta}\right)^{3+\alpha}. \tag{9}$$

From X-ray observations $\alpha \approx 0.9$ and $R \geq 10$ at the brightest part of the X-ray jet. Assuming $\theta > 23^\circ$ (section 4.1), then $\beta > 0.3$. This is approximately three times larger than the inferred average recessional speed of hot spots from the nucleus. If the X-rays are the result of inverse Compton scattering of the microwave background radiation, the exponent $3{+}\alpha$ in equation (9) becomes $4{+}2\alpha$ (cf. equation 6) and a somewhat smaller lower limit to β is obtained.

5. Concluding Remarks

Our Chandra study of Pictor A has shown that the X-ray emissions from the jet and the western hot spot are non-thermal. The spectra of both are well described by an absorbed power law with (flux density) spectral index $\alpha \simeq 1.0$. The X-ray spectrum of the hot spot is not a smooth extension of the radio to optical synchrotron spectrum, which turns down or cuts off near $\sim 10^{14}$ Hz. Inverse Compton scattering of the synchrotron radio photons by the relativistic electrons responsible for the radio emission (i.e. a synchrotron self-Compton model) may be ruled out for the hot spot's X-ray emission, as the predicted spectrum differs from that observed. Inverse Compton scattering is also an unlikely explanation for the X-ray emission of the jet, for it requires a magnetic field a factor of 30 below equipartition. Further, it is hard to understand why the jet is brighter than the lobe (the opposite of the situation in the radio) in an inverse Compton scenario.

We considered the possible existence of a population of relativistic electrons in the hot spot that radiates synchrotron emission at frequencies below that at which its spectrum has been measured (i.e. < 327 MHz). By choosing an appropriate index for the energy spectrum of these electrons, we constructed a successful synchrotron self-Compton model for the X-rays at the price of reducing the magnetic field to $\sim 1\%$ of equipartition (see Fig. 9 and Model 3 in Table 4). More generally, relativistic electrons could exist in regions with weak or absent magnetic fields. Since the properties of such electron populations are unconstrained by radio observations, one can always create inverse Compton models that match the X-ray spectra. It is, however, difficult to understand why the X-rays from both the jet and the hot spot should correlate so well with synchrotron radio emission, which must arises in a relatively strong magnetic field. In general, we consider inverse Compton models for the X-ray emission as implausible.

The X-ray spectrum of the hot spot may be reproduced in a composite synchrotron plus synchrotron self-Compton model. In this picture, the spectral index of the synchrotron radiation is supposed to increase by 0.5 above the break near 10^{14} Hz, as would be expected in a continuous injection model. Addition of this synchrotron emission to the synchrotron self-Compton emission expected for a magnetic field a factor of 9 below equipartition reproduces the observed spectrum (see Fig. 8 and Model 2, Table 4). The model is contrived, requiring similar fluxes from the two components in the Chandra band, but cannot be ruled out.

We feel that synchrotron radiation is the most likely X-ray emission process of both jet and hot spot. Strong, non-relativistic shocks are believed to accelerate relativistic particles yielding an energy spectrum $n(E) \propto E^{-p}$ with $p = 2$ at injection. Since the half lives of X-ray emitting electrons to synchrotron losses are very short ($\sim$ years), the spectrum steepens and a synchrotron spectral index of $\alpha = 1.0$ is expected, in excellent accord with observations (Models 4a, b, Table 4). The separate population of radio-optical synchrotron emitting electrons remains unexplained; the radio spectral index - $\alpha_r = 0.740 \pm 0.015$ - is close to the average for non-thermal radio sources. Various processes, including acceleration in weak shocks, synchrotron losses and effects of tangled fields (see summary in Longair 1994, Ch. 21), have been invoked to account for the difference between the typical index seen in radio sources and the value $\alpha = 0.5$ expected in the canonical model. Hot spots are, of course, associated with two shocks - an internal, mildly relativistic shock in the jet and a non-relativistic bow shock in the intergalactic medium. Both may reasonably be expected to accelerate cosmic rays and the resulting fluxes and energy spectra may differ.

As well as being directly accelerated in shocks, high γ relativistic electrons may result from a 'proton induced cascade' initiated by photopion production (e.g. Sikora et al. 1987; Biermann & Strittmatter 1987; Mannheim & Biermann 1989; Mannheim, Krülls & Biermann 1991). In this process, relativistic proton - photon collisions create π^0, π^+ and π^-. The last two decay into relativistic electrons, positrons, neutrinos and antineutrinos (e.g. Biermann & Strittmatter 1987). The process thus provides a supply of synchrotron X- and γ-ray emitting electrons and positrons from high energy protons accelerated by shocks. Mannheim, Krülls & Biermann (1991) considered this process for production of synchrotron X-ray emission in radio galaxy hot spots. Their calculations suggest that the proton induced cascade produces X-ray emission about an order of magnitude weaker and with a harder spectrum than is observed for the western hot spot of Pictor A. As they note, the predicted luminosity can be increased by increasing the number of relativistic protons or the number of photons (the latter might occur, for example, if the hot spot is illuminated by a beam of radiation from the galaxy nucleus). This process seems promising and further calculations of the expected X-ray luminosity and spectrum of a proton induced cascade would be worthwhile.

This research was supported by NASA through grant NAG 81027. We are extremely grateful to Rick Perley for providing the radio images published by PRM in numerical form. We also wish to thank the staff of the Chandra Science Center, especially Dan Harris and Shanil Svirani, for their help.

REFERENCES

Arshakian, T. G. & Longair, M. S. 2000, MNRAS, 311, 846

Band, D.L., & Grindlay, J.E. 1985, ApJ, 298, 128

Band, D.L., & Grindlay, J.E. 1986, ApJ, 308, 576

Begelman, M. C., Blandford, R. D. & Rees, M. J. 1984, Rev. Mod. Phys. 56, 255

Begelman, M. C. & Sikora, M. 1987, ApJ, 322, 650

Bell, A. R. 1978, MNRAS, 182, 147

Biermann, P. L. & Strittmatter, P. A. 1987, ApJ, 322, 643

Blandford, R. D. & Ostriker, J. P. 1978, ApJ, 221, L29

Blumenthal, G. R. & Gould, R. J. 1970, Rev. Mod. Phys., 42, 237

Bridle, A. H. 1996, In Energy Transport in Radio Galaxies and Quasars, ASP Conference Series Vol. 100, eds. P. E. Hardee, A. H. Bridle and J. A. Zensus, p 383 (Astronomical Society of the Pacific: San Francisco)

Clarke, D. A., Harris, D. E. & Carilli, C. L. 1997, MNRAS, 284, 981

Danziger, I. J., Fosbury, R. A. E. & Penston, M. V. 1977, MNRAS, 179, 41P

de Young, D. S. 1986, ApJ, 307, 62

Dermer, C. D. 1995, ApJ (Letts), 446, L63

Eracleous, M. & Halpern, J. P. 1998, ApJ, 505, 577

Eracleous, M., Sambruna, R. & Mushotzky, R. F. 2000, ApJ, 537 (in press for July 10 issue)

Halpern, J. P. & Eracleous, M. 1994, ApJ, 433, L17

Harris, D. E., Carilli, C. L. & Perley, R. A. 1994, Nature, 367, 713

Heiles, C. & Cleary, M.N. 1979, Australian J. Phys. Astrophys. Suppl., 47, 1

Jones, P. A., McAdam, W. B., & Reynolds, J. E. 1994, MNRAS, 268, 602

Kardashev, N. S. 1962, Sov. Astr. (AJ), 6, 317

Laing, R. A. 1988, Nature, 331, 149

Longair, M. S. 1994, High Energy Astrophysics, Volume 2 (Cambridge University Press)

Mannheim, K. & Biermann, P. A. 1989, A&A, 221, 211

Mannheim, K., Krülls, W. M. & Biermann, P. L. 1991, A&A, 251, 723

Meisenheimer, K., Yates, M. G. & Röser, H-J. 1997, A&A, 325, 57

Padovani, P., Morganti, R., Siebert, J., Vagnetti, F. & Cimatti, A. 1999, MNRAS, 304, 829

Rees, M. J. 1967, MNRAS, 137, 429

Perley, R. A., Röser, H-J. & Meisenheimer, K. 1997, A&A, 328, 12 (PRM)

Robertson, J. G. 1973, Aust J Phys, 26, 403

Röser, H-J. & Meisenheimer, K. 1987, ApJ, 314 70

Röser, H-J. 1989, in Lecture Notes in Physics vol. 327, Hot Spots in Extragalactic Radio Sources, eds. Meisenheimer, K., & Röser, H.-J., Springer-Verlag, p. 91

Rybicki, G. B. & Lightman, A. P. 1979, Radiative Processes in Astrophysics, p 207 (John Wiley & Sons)

Schmidt, M. 1965, ApJ, 141, 1

Sikora, M., Kirk, J. G., Begelman, M. C. & Schneider, P. 1987, ApJ, 320, L81

Simkin, S. M., Sadler, E. M., Sault, R., Tingay, S. J. & Callcut, J. 1999, ApJS, 123, 447

Storchi-Bergmann, T., Eracleous, M., Ruiz, M. T., Livio, M., Wilson, A. S. & Filippenko, A. V. 1997, ApJ, 489, 87

Sulentic, J. W., Marziani, P., Zwitter, T. & Calvani, M. 1995, ApJ, 438, L1

Thomson, R. C., Crane, P. & Mackay, C. D. 1995, ApJ, 446, L93

Tingay, S. J. et al. 2000, AJ, 119, 1695

Urry, C. M. & Padovani, P. 1995, PASP, 107, 803

Worrall, D. M. & Birkinshaw, M. 2000, ApJ, 530, 719

Table 1. Spectral Fits to the X-ray Emission of the Western Hot Spot[a]

Model	$N_{\rm H}$ [$\times$ 10^{20} atoms cm^{-2}]	kT [keV]	Metal Abundance	K$_1^{\rm b}$	$\Gamma^{\rm c}$	K$_2^{\rm d}$	χ^2/dof
Raymond-Smith	$0.0^{+0.2}_{-0.0}$	$4.8^{+0.6}_{-0.3}$	solar	$(3.44^{+0.12}_{-0.12}) \times 10^{-4}$	–	–	166 / 97
Raymond-Smith	4.2 (frozen)	$4.7^{+0.4}_{-0.4}$	solar	$(3.9^{+0.1}_{-0.1}) \times 10^{-4}$	–	–	232 / 99
Raymond-Smith	$0.0^{+1.3}_{-0.0}$	$3.5^{+0.4}_{-0.4}$	$0.0^{+0.1}_{-0.0}\times$ solar	$(4.57^{+0.28}_{-0.21}) \times 10^{-4}$	–	–	101 / 96
Raymond-Smith	4.2 (frozen)	$2.7^{+0.3}_{-0.3}$	$0.00^{+0.04}_{-0.0}\times$ solar	$(5.7^{+0.2}_{-0.3}) \times 10^{-4}$	–	–	122 / 98
Power Law	$7.1^{+2.3}_{-2.3}$	–	–	–	$2.07^{+0.11}_{-0.11}$	$(1.34^{+0.13}_{-0.11}) \times 10^{-4}$	95 / 98

[a]Errors are 90% confidence

[b]$K_1 = 10^{-14} \int n_e n_H dV/4\pi D^2$, where D is the luminosity distance to the source (cm), n_e is the electron density (cm^{-3}) and n_H is the hydrogen density (cm^{-3}).

[c]Γ is the photon index.

[d]K_2 is the number of photons keV^{-1} cm^{-2} s^{-1} at 1 keV

Table 2. Spectral Fits to the X-ray Emission of the Jet[a]

Model	N_{H} [$\times$ 10^{20} atoms cm^{-2}]	kT [keV]	Metal Abundance	K_1	Γ	K_2	χ^2/dof
Raymond-Smith	4.2 (frozen)	$3.7^{+1.6}_{-1.1}$	solar	$(4.4^{+7.6}_{-0.9}) \times 10^{-5}$	–	–	27 / 15
Raymond-Smith	4.2 (frozen)	$2.2^{+1.3}_{-0.6}$	$(0.0^{+0.3}_{-0.0})\times$ solar	$(6.7^{+1.3}_{-1.6}) \times 10^{-5}$	–	–	19 / 14
Power Law	$5.8^{+6.8}_{-5.6}$	–	–	–	$1.94^{+0.43}_{-0.49}$	$(1.45^{+0.62}_{-0.36}) \times 10^{-5}$	15 / 14

[a]Parameters and errors are as defined in the footnotes to Table 1

Table 3. Parameters of, and within, the Western Hot Spot

L(327 MHz - optical)	$\simeq 3 \times 10^{43}$ erg s^{-1}
L(0.1 - 10 keV)	4.9×10^{42} erg s^{-1}
H_{eq} (bright core)	4.7×10^{-4} gauss
H_{eq} (filament)	9.1×10^{-5} gauss
ϵ_{rad} (core, synchrotron rad'n)	$\sim 8 \times 10^{-12}$ erg cm^{-3}
ϵ_{rad} (filament, synchrotron rad'n)	$\sim 1 \times 10^{-13}$ erg cm^{-3}
ϵ_{rad} (microwave background)	4×10^{-13} erg cm^{-3}
ϵ_{rad} (galaxy optical light)	4×10^{-16} erg cm^{-3}

Table 4. Parameters of the Models of the Western Hot Spot

Model	n_{e_0} [cm^{-3}]	p	$\gamma_{\rm min}$	$\gamma_{\rm break}$	$\gamma_{\rm max}$	Radius [cm]	Magnetic Field [gauss]	Fraction of equipartition field
1	5.3	2.48	8.7×10^1	–	–	7.7×10^{20}	3.3×10^{-5}	0.07
2	2.2	2.48	8.7×10^1	4.75×10^5	–	7.7×10^{20}	5.3×10^{-5}	0.11
3	485.0	3.30	1.0×10^2	–	9×10^3	7.7×10^{20}	2.8×10^{-6}	0.01
4a	1.0×10^{-3}	2.14	–	5×10^4	–	7.7×10^{20}	4.7×10^{-4}	1
4b	1.2×10^{-5}	2.14	–	4×10^6	–	7.7×10^{20}	4.7×10^{-4}	1

Table 5. Estimated Parameters within the Jet[a]

H_{eq}	2.3×10^{-5} $(r_j/1 \text{ arc sec})^{-4/7}$ gauss
ϵ_{rad} (synchrotron rad'n)[b]	$\sim 1 \times 10^{-15}$ $(r_j/1 \text{ arc sec})^{-1}$ erg cm^{-3}
ϵ_{rad} (microwave background)	4×10^{-13} erg cm^{-3}
ϵ_{rad} (galaxy optical light)	$\sim 8 \times 10^{-15}$ $(R/1 \text{ arc min})^{-2}$ erg cm^{-3}

[a] r_j is the angular radius of the synchrotron emitting region of the jet, and R is the distance of the region of the jet from the galaxy.

[b] Assumes an upper cut-off frequency of $\nu_{max} = 10^{11}$ Hz for the synchrotron spectrum. ϵ_{rad} (synchrotron rad'n) should be multiplied by 3.1 if $\nu_{max} = 10^{14}$ Hz and by 11.5 if $\nu_{max} = 10^{18}$ Hz.

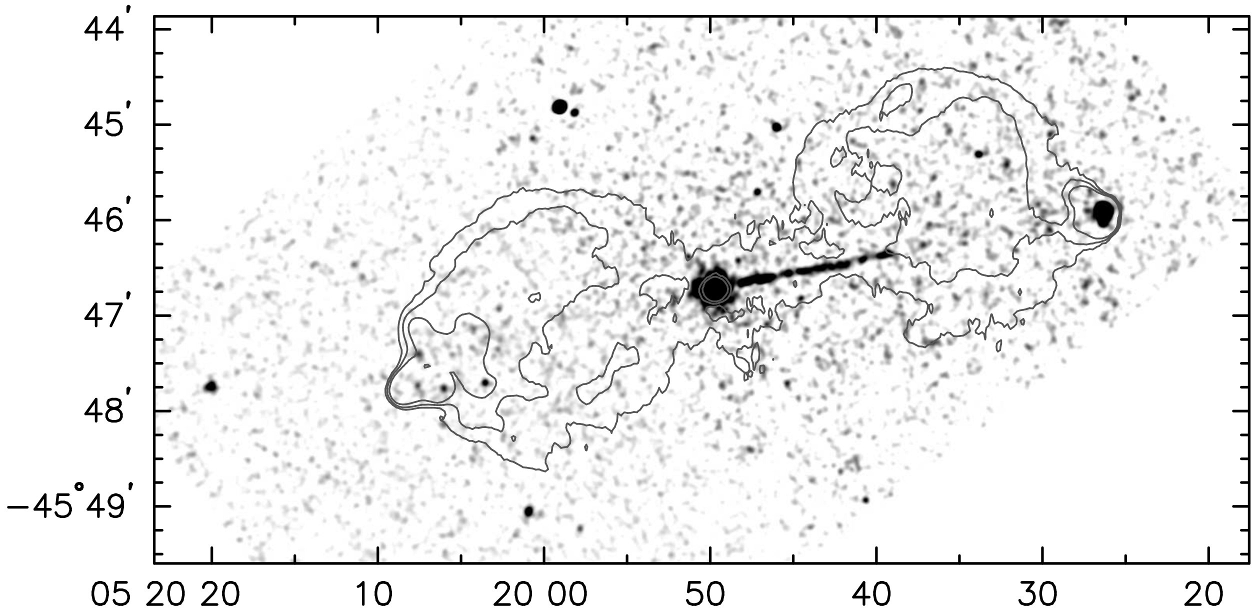

Fig. 1.— Large field image of the X-ray emission from Pictor A, processed as described in Section 2.1. Coordinates are for epoch J2000.0. A smoothing of $\sigma = 1''.0$, in addition to that described in Section 2.1, has been applied, so the FWHM resolution is $\simeq 3''.4$. Three contours of the $7''.5$ resolution 20 cm radio image of PRM are shown; they represent 0.025, 0.05 and 0.1 Jy (beam area)$^{-1}$. The following X-ray features are noteable: a) the bright X-ray source associated with the nucleus; b) the $1'.9$ long X-ray jet extending to the W; c) the western hot spot $4'.2$ from the nucleus; d) possible faint, diffuse X-ray emission around the galaxy on the $1'$ scale; e) faint X-ray emission extending from the nucleus to the eastern hot spots; f) four compact X-ray sources within the uppermost radio contour around the eastern hot spot; and g) an X-ray source near the eastern edge of the frame which, with respect to the nucleus, is aligned in a direction precisely opposite to that from the nucleus to the western hot spot.

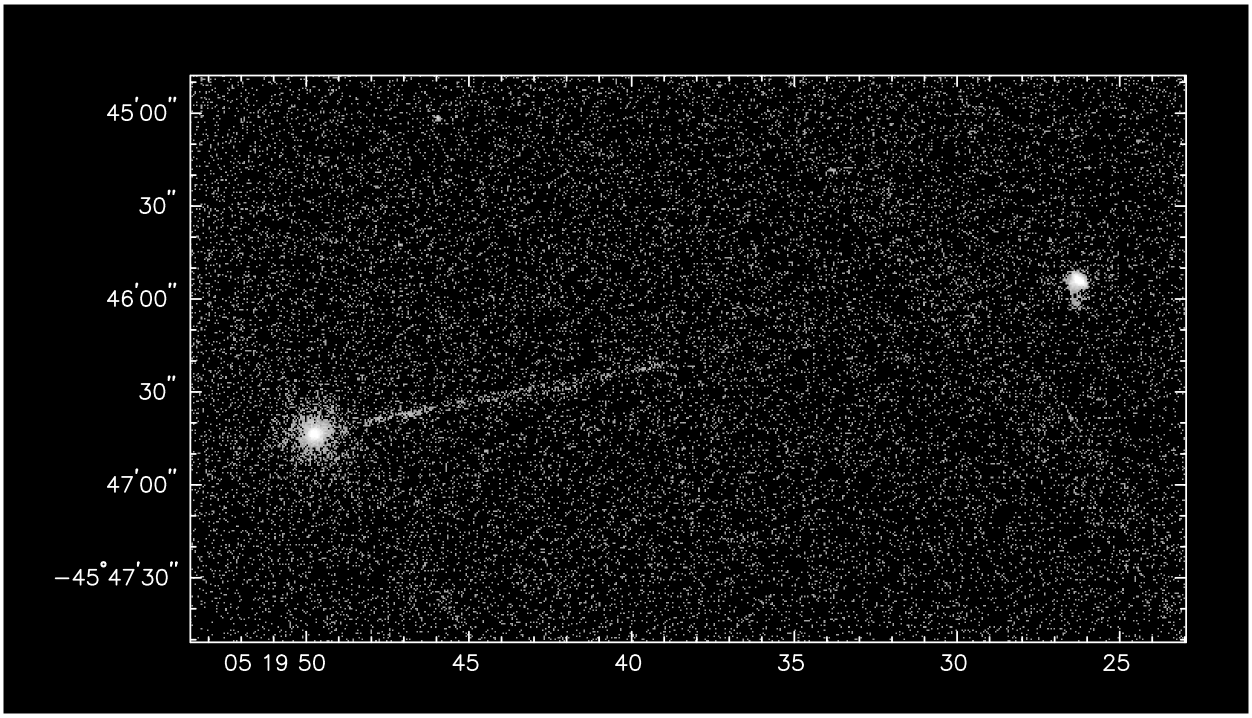

Fig. 2.— Grey scale representation of the full resolution Chandra image of the nucleus, jet and western hot spot of Pictor A.

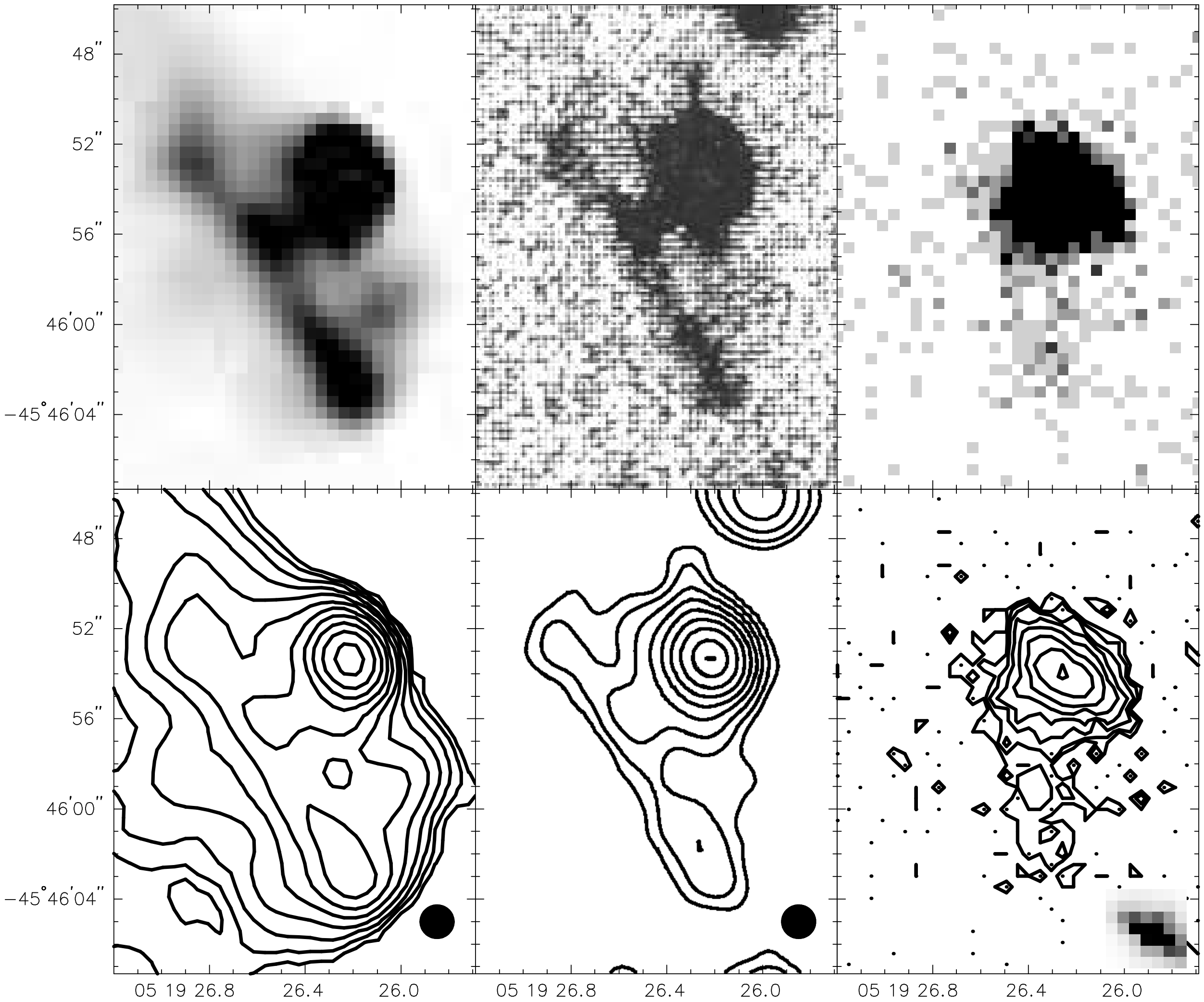

Fig. 3.— The morphology of the western hotspot of Pictor A, at 3.6 cm radio (left panels; PRM), R band optical (center panels; Röser (1989) and PRM) and X-ray (right panels; this paper) wavelengths. The upper panels are grey scale representations and the lower panels are contour plots in which the contours are logarithmically spaced and separated by a factor of 2. The radio and optical images have a FWHM resolution $\simeq 1\farcs5$ (shown as the filled circles at the bottom right) and the X-ray image has a FWHM of $1\farcs2 \times 1\farcs9$ (the PSF is shown at the bottom right; no smoothing has been applied to the X-ray image). The coordinates are for epoch J2000.0

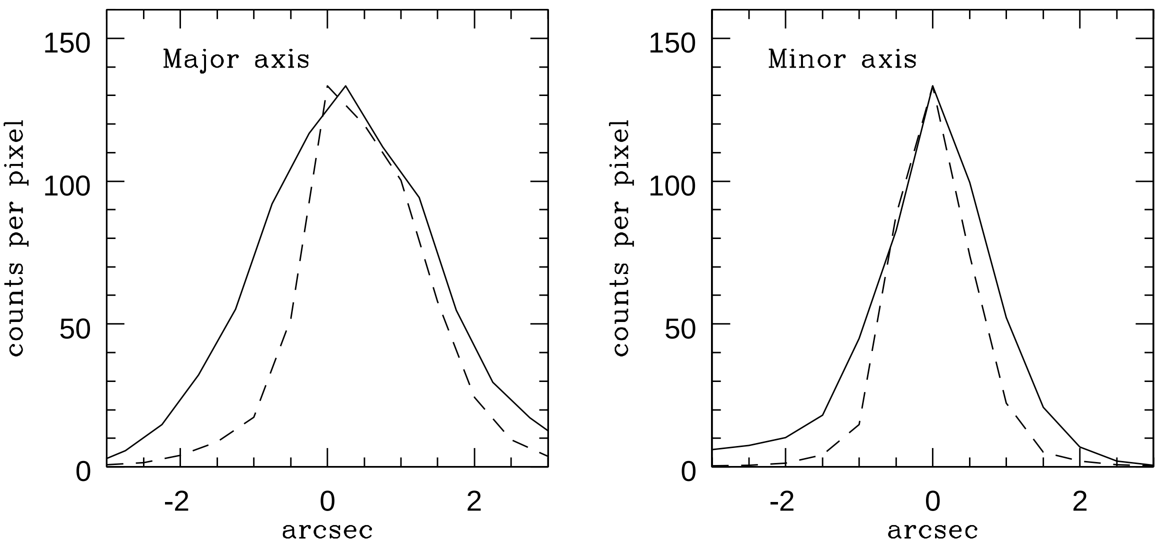

Fig. 4.— Profiles of the X-ray emission (solid lines) through the peak of the western hot spot along its major axis (p.a. $\simeq 47^{\circ}$, left panel) and perpendicular to that direction (right panel). Profiles through the model psf at the location of the hot spot in the same directions are shown as dashed lines.

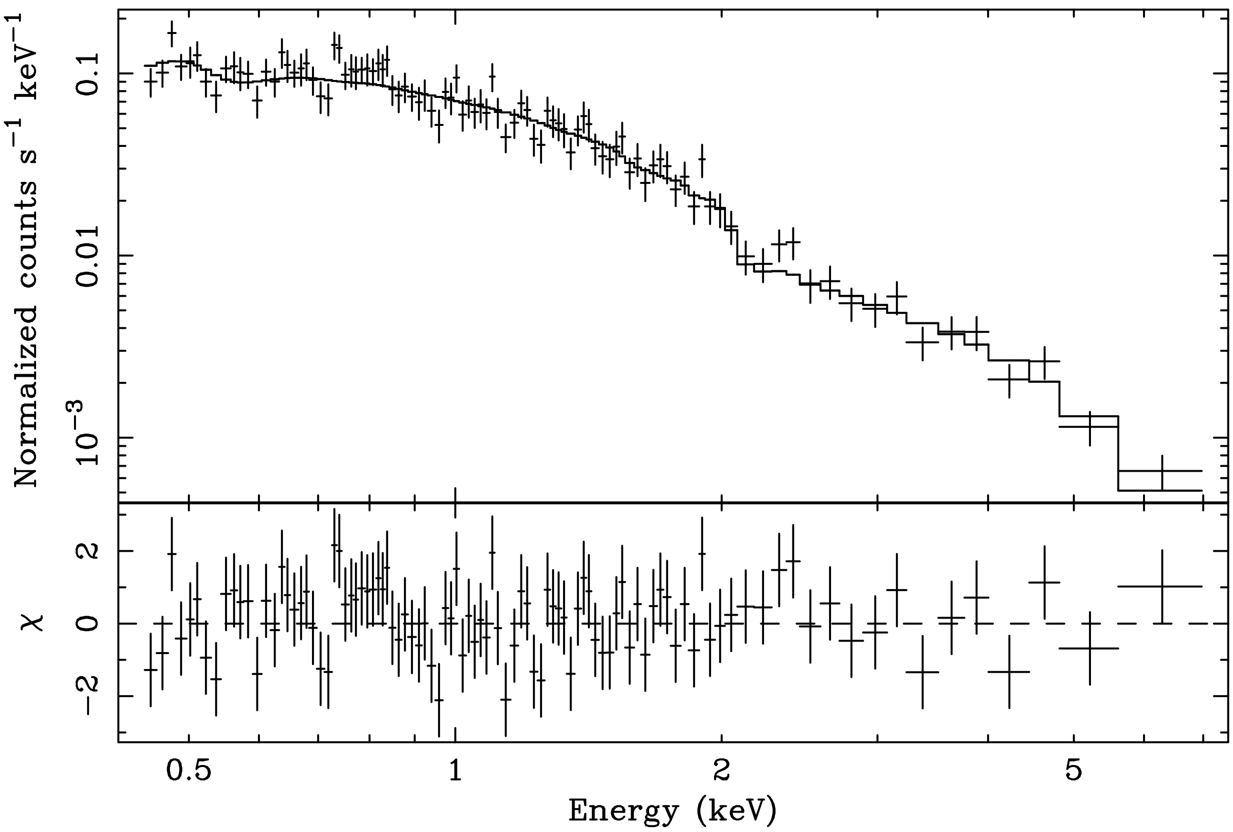

Fig. 5.— The X-ray spectrum of the western hot spot of Pictor A. The upper panel shows the observed count rate on the detector (crosses), and the best model of an absorbed power law folded through the instrumental response (solid line). The parameters of this model are given in Table 1. The lower panel shows the χ residuals from this fit.

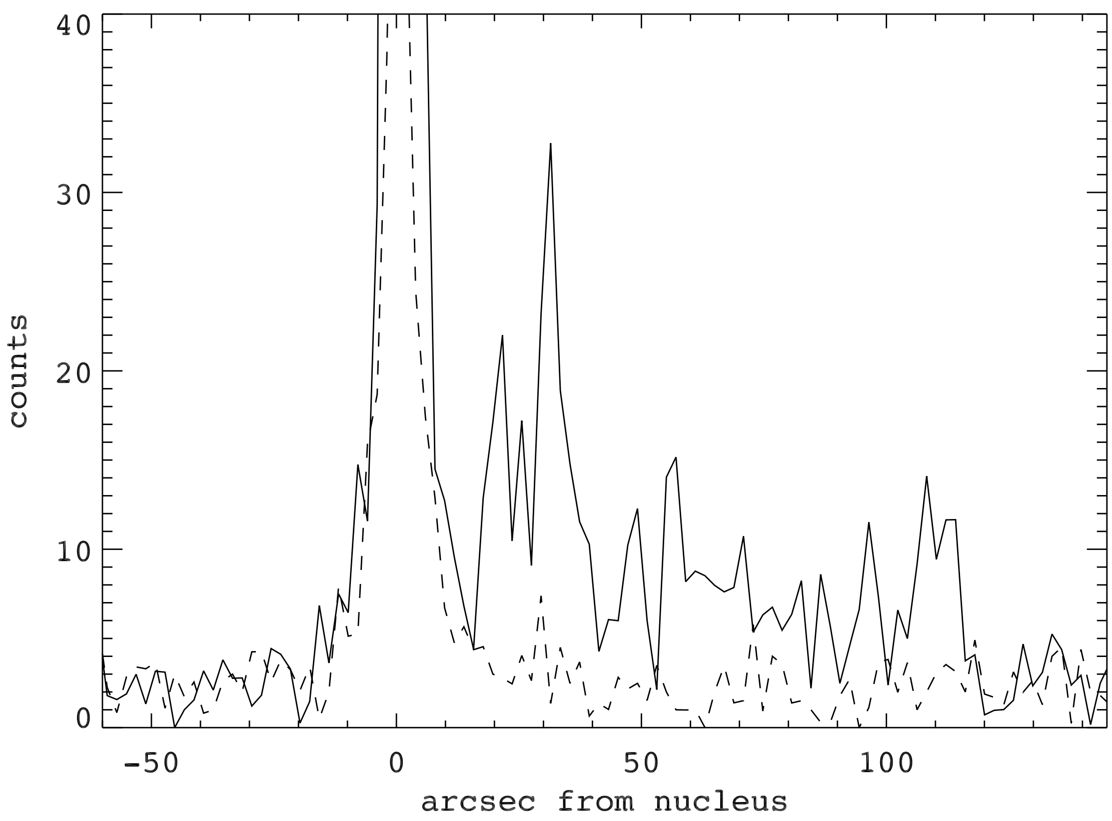

Fig. 6.— Profiles of the X-ray emission along the jet (solid line) and a background region offset from the jet (dotted line). Radial distance from the nucleus increases to the west. Counts from the jet were summed over 2″ bins in the radial direction and 2.″5 bins in the transverse direction. A similar region was used for the background, offset from the jet by 2.″5 in the transverse direction. Excess X-ray emission from the jet is clearly seen on the western side of the nucleus out to 1.′9, whereas there is no evidence of X-ray emission from a jet to the east of the nucleus.

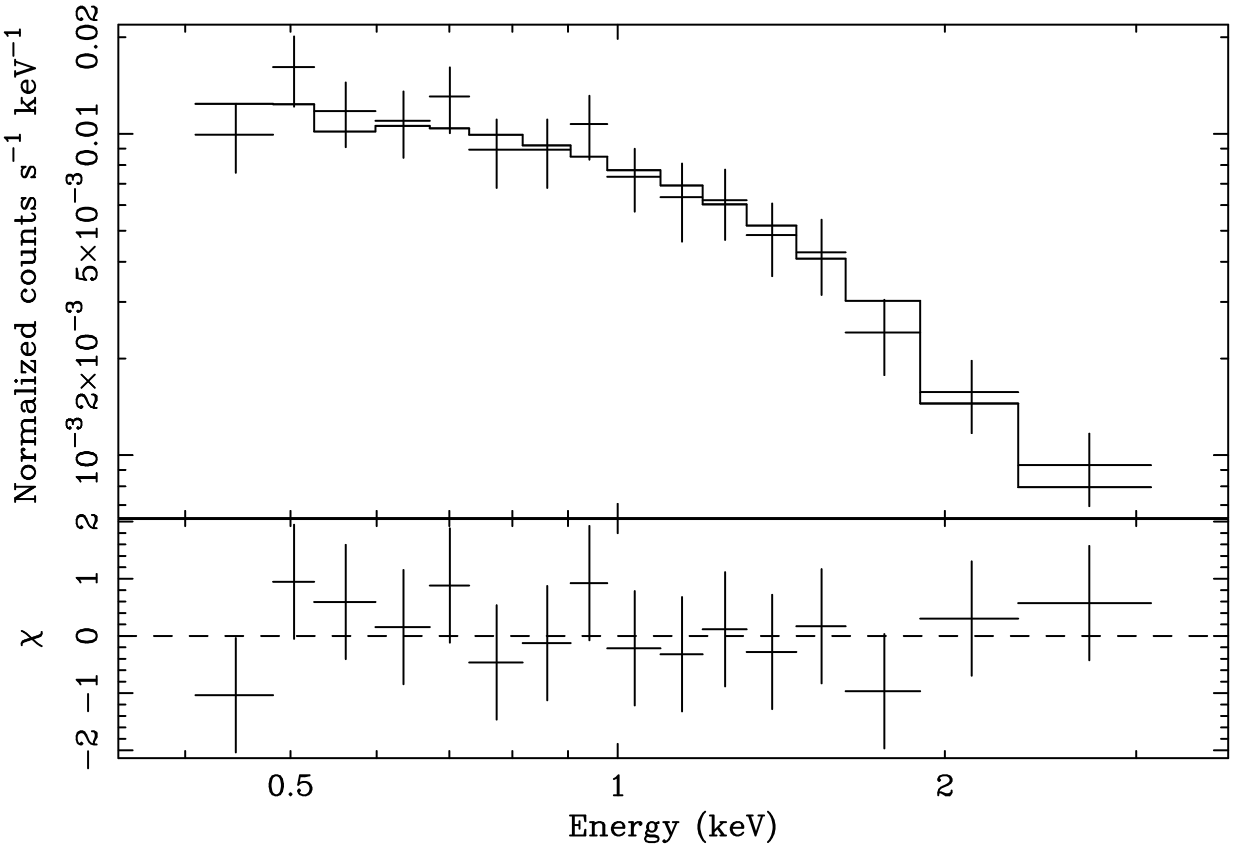

Fig. 7.— The X-ray spectrum of the jet of Pictor A. The upper panel shows the observed count rate on the detector (crosses), and the best model of an absorbed power law folded through the instrumental response (solid line). The parameters of this model are given in Table 2. The lower panel shows the χ residuals from this plot.

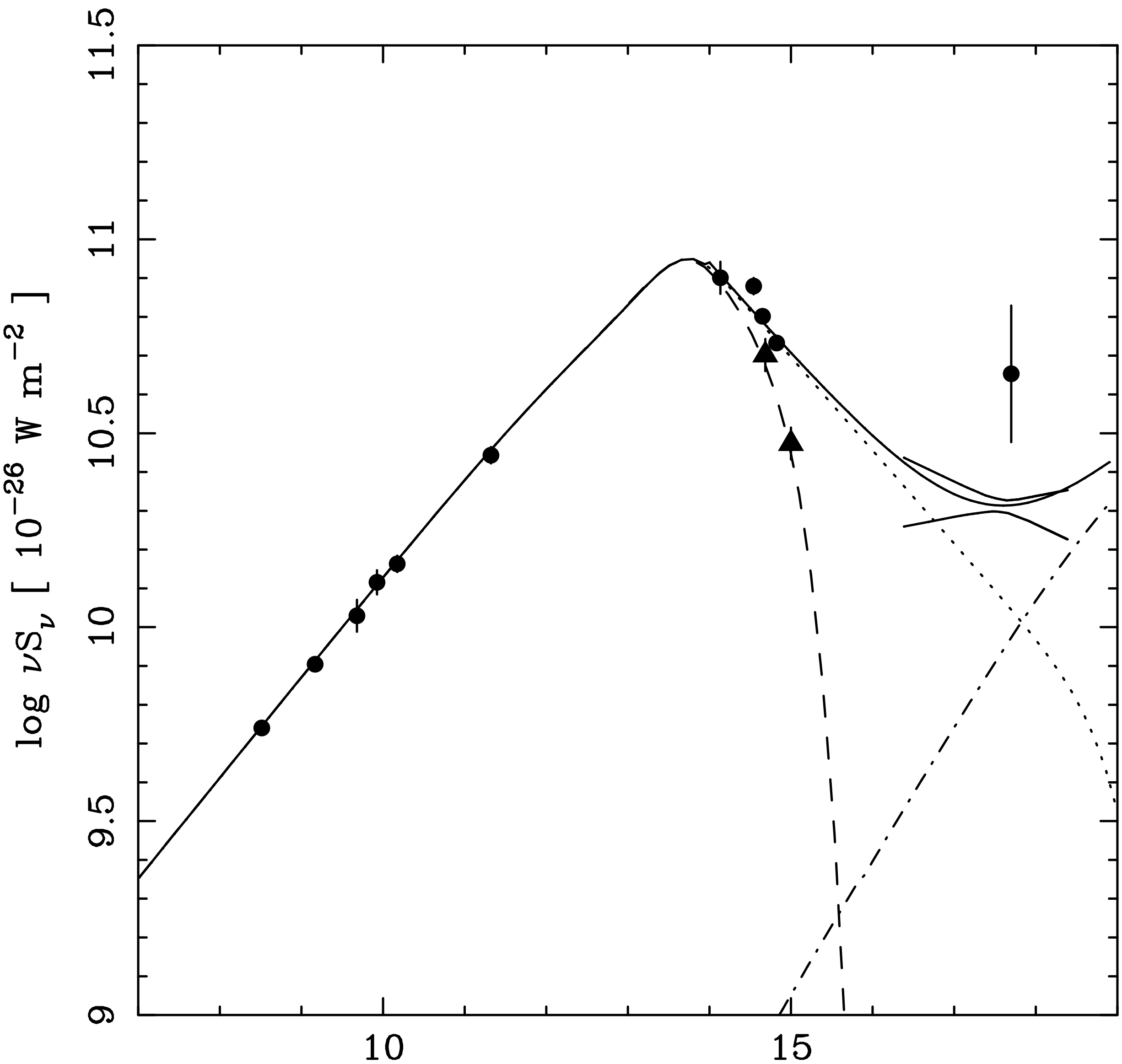

Fig. 8.— The broad band spectrum, plotted as νS_ν, of the western hotspot of Pictor A from radio through to X-ray wavelengths. All the radio points and most of the near infrared and optical are taken from Meisenheimer, Yates & Röser (1997). The two optical/near ultraviolet points (represented by triangles) come from our analysis of archival HST observations of the hot spot (Section 2.2). The X-ray point with large error bars is from the Einstein Observatory (Röser & Meisenheimer 1987). The "bow tie" represents the spectral range allowed by the Chandra observations. The other lines represent models, as follows. The solid curve called, model 2 in the text, is the sum of synchrotron emission (passing through the radio data points and breaking at $\sim 10^{14}$ Hz due to synchrotron losses; dotted line) and a synchrotron self-Compton component (dot-dashed line). The dashed line shows the synchrotron spectrum expected from a sharp cut-off in the energy spectrum of the electrons at $\gamma \simeq 5 \times 10^5$ in the equipartition magnetic field of 4.7×10^{-4} gauss (Table 3).

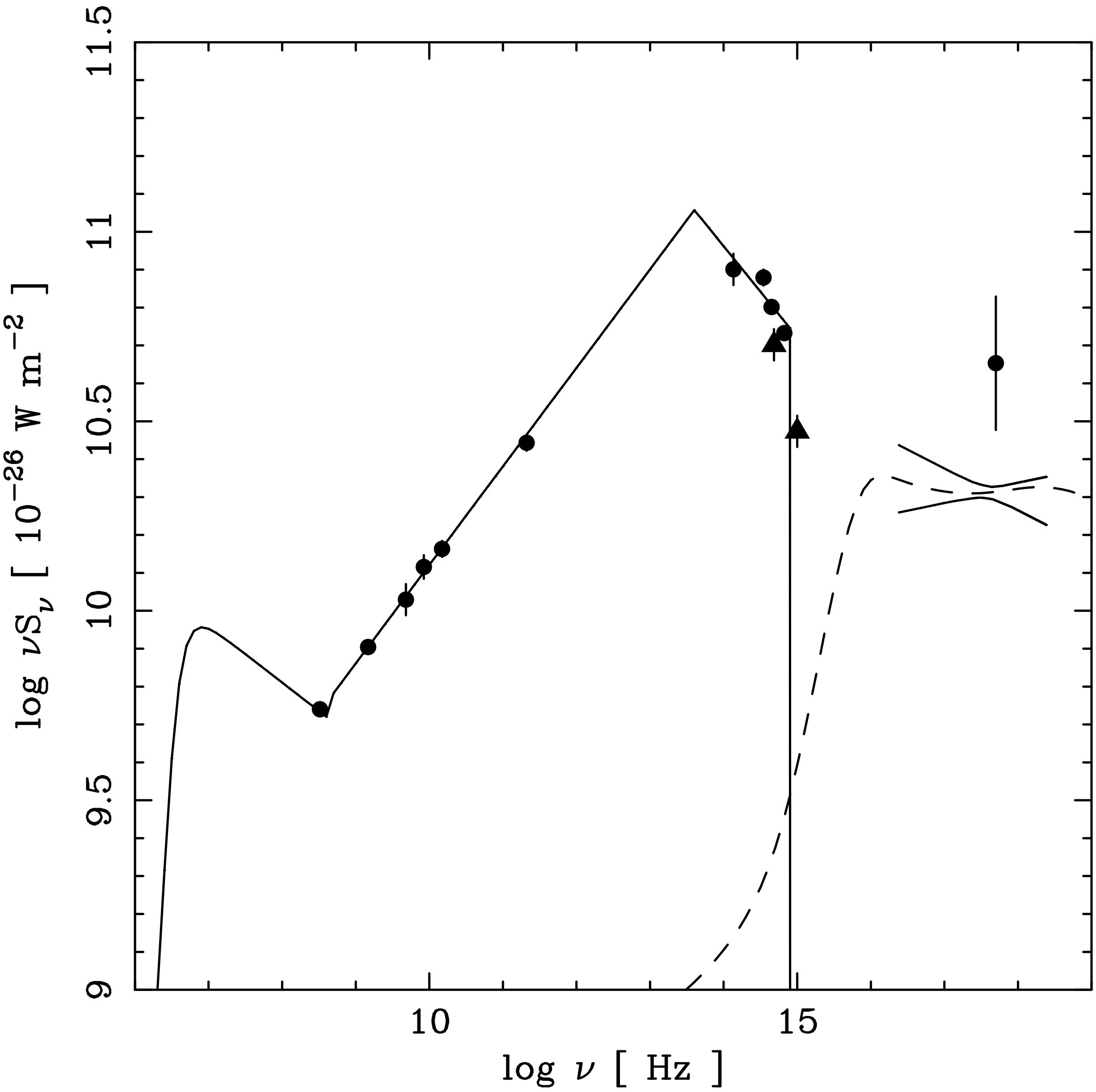

Fig. 9.— The observed spectrum of the western hot spot with the addition of a hypothetical low frequency (< 327 MHz) radio synchrotron component. Inverse Compton scattering of the radio-optical photons by the hypothesised low energy electron population produces an X-ray spectrum (dashed line) compatible with the Chandra-measured spectrum shown as the 'bow tie' (model 3; See Section 4.2.2 and Table 4).